Fast and Extensive Intercalation Chemistry in Wadsley-Roth Phase Based High-Capacity Electrodes

Miao Wang[1,2&], Zhenpeng Yao[3,5&], Qianqian Li[4&], Yongfeng Hu[6], Jing Zhang[1], Jiujun Zhang[1], Yufeng Zhao[1,2]*, Alán Aspuru-Guzik[3,5,7,8]

[1] *Institute for Sustainable Energy & College of Sciences, Shanghai University, Shanghai 200444, China*
[2]*Key Laboratory of Applied Chemistry, Yanshan University, Qinhuangdao 066004, China*
[3]*Department of Chemistry and Chemical Biology, Harvard University, 12 Oxford Street, Cambridge, Massachusetts 02138, United States*
[4]*Materials Genome Institute, Shanghai University, Shanghai 200444, China*
[5]*Chemical Physics Theory Group, Department of Chemistry and Department of Computer Science, University of Toronto, Toronto, Ontario M5S 3H6, Canada*
[6]*Canadian Light Source, 44 Innovation Boulevard, Saskatoon, SK, S7N 2 V3, Canada*
[7]*Vector Institute for Artificial Intelligence, Toronto, Ontario M5S 1M1, Canada*
[8]*Canadian Institute for Advanced Research (CIFAR) Lebovic Fellow, Toronto, Ontario M5S 1M1, Canada*
[&] *These authors contribute equally to this work.*
Corresponding email：yufengzhao@shu.edu.cn

Abstract

Wadsley-Roth (W-R) structured oxides featured with wide channels represent one of the most promising material families showing compelling rate performance for lithium ion batteries. But the structural origin for the fast kinetics of W-R structures is not well understood. Herein, we report an in-depth study on the fast and extensive intercalation chemistry of phosphorus stabilized W-R phase PNb_9O_{25} and its application in high energy and fast-charging devices. We survey all the known W-R structures and identify their intercalation geometry. We are able to construct a connection between the cavity number of a structure and its capability upon accommodating lithium ions. Using this rule, we identify two geometrical types of stable insertion sites in PNb_9O_{25} structure with the total amount (2.22 per Nb ion) and a measured remarkable high reversible capacity. A remarkable cycling stability is observed with 90% capacity retention after 1100 cycles at 7.2C. We reveal the ion transportation kinetics that the Li ions initially diffuse along the open type III channels and then penetrate to type-α edge sites with low kinetic barriers. Through *in-situ* TEM and *ex-situ* XRD investigations, we confirm

that the whole intercalation/deintercalation process proceeds *via* a solid-solution behavior with continuous lithium (de)occupying/(re)ordering on the identified insertion sites exhibiting nearly "zero-stress" characteristics.

Introduction

Lithium ion battery (LIB), the technique which enabled the wireless evolution, is now gaining a significant amount of attention for its applications in sustainable transportation and large-scale renewable energy storage fields.[1-3] LIBs armed with high energy density and, especially, high rate capability electrodes, are considered to be the ideal on-board energy storage solution for the electric vehicles and plugin hybrid vehicles (EVs and PHEVs), as well as many other emerging power-intensive devices.[4,5] Unlike the development of electrodes targeted on higher capacity and operation voltage, which has gone through several notable generations (*e.g.*, $LiCoO_2$,[6] $LiFePO_4$,[7] $LiNi_xMn_yCo_{1-x-y}O_2$,[8] anionic redox active materials,[9,10] Si,[11] and so on), the pursuit of high rate electrode materials is still ongoing, especially on the anode side.[12,13] Carbonaceous materials (*e.g.*, graphite) which have been employed since the first commercialization of LIBs, are proven to be inadequate for high rate usage.[14,15] Besides, their intrinsically low Li-ion accommodation/ extraction voltages lead to a strong tendency of Li-plating on the electrode surface and increased risk of dendrite formation at high current densities, which will then cause potential cell short circuit and fire hazards.[16] Transition metal oxides (TMOs) based intercalation-type electrodes like $Li_4Ti_5O_{12}$ (LTO),[17] have been well-known for their superior Li ionic conductivity. LTO based electrode aided by nanosized carbon coatings can maintain a capacity around 150 mAh/g at a rate as high as 10 C with remarkable cyclability and constrained volume variation.[18] Li (de-)intercalate into LTO at a much higher voltage (~1.55 V) compared to graphite, preventing the Li plating and increasing battery safety. However, the high operation voltage of LTO also leads to a reduced output voltage of the full cell. Meanwhile, limited amount of Li insertion sites in LTO structure intrinsically constrains its capability to accommodate Li ions. As a result, energy density of the LTO based full cell is significantly compromised. Therefore, efforts are still being made on the search of electrode materials with fast Li transport, large capacity, strong electrochemical stability, minor volume expansion as well as modestly 'high' operation voltage for next-generation batteries.

Wadsley-Roth (W-R) oxides are one of the most promising fast rate material families for LIBs, exhibiting great potential to realize extensive intercalation chemistry because of the featured wide channels in their structures. W-R phases are generally ReO_3-derivated structures with re-organized ReO_3-type blocks (MO_6 octahedra) through edge-sharing only or combined edge-sharing and corner-sharing *via* tetrahedrally coordinated metal atoms (**Figure. 1A**). A W-R structure then can be defined by the way it is built: $n \times m \times \infty$ with n and m stand for the number of octahedra in-plane and ∞ standing for the infinite layer stacking in the perpendicular direction.[19] The original ReO_3 structure is highly symmetric featured with large cavities (type I) because of the empty cationic A sites (**Figure. 1A**). Therefore, it drew great attention from the battery field for the exploration of possible reversible and extensive Li intercalation. However, pure ReO_3 structure is found to be unstable upon limited lithiation followed by a series of phase transformation.[19] Compared with the corner-sharing-only shaky structure of original ReO_3, the W-R structures are denser packed as a result of the introduction of edge-sharing connection and a fraction of the cavities are then occupied by octahedra/tetrahedra (**Figure. 1A**), leading to the remarkably improved structural stability upon ion intercalation. Meanwhile, partially preserved large cavities (type I-V, **Figure. 1A, B**) of the W-R structure show great promises for enabling the fast ionic transport. The combination of these two merits makes W-R phases extremely compelling for the application of fast and high-capacity electrodes for Li-ion batteries.[20-29] To date, many W-R oxides have been reported as fast rate electrodes like T-Nb_2O_5,[20] TT-Nb_2O_5,[21] $TiNb_2O_7$,[22,23] $Nb_{12}WO_{33}$,[24] $Nb_{16}W_5O_{55}$,[25] PNb_9O_{25},[26] $Nb_{14}W_3O_{44}$,[27] and $Nb_{18}W_8O_{69}$[28] and $Ti_2Nb_{10}O_{29-x}$.[29] However, the structural origin of the fast and extensive intercalation chemistry of the W-R structures is still unclear and thus calls for further investigation.

Herein, we revisit the phosphorus stabilized W-R phase PNb_9O_{25}, which featured with stable open channels, as intercalation-type electrode for boosted Li-ion storage. We report the excellent rate performance (392 mAh/g at 0.48 C, 253 mAh/g at 4.8 C) and remarkable cycling stability (90% retention after 1100 cycles at 7.2C) of PNb_9O_{25}@CNTs composite electrode in half-cell, and a record high energy density in full-cell (333.5 Wh/kg based on total mass of both electrodes). We provide an in-depth study on the lithiation reaction mechanism *via* density functional theories (DFT) calculations combined with *in-situ* TEM and *ex-situ* XRD analysis. The intercalation geometry of PNb_9O_{25} is identified with 20 insertion sites per formula unit (f.u.) and the nearly "zero-stress" characteristic. The Li-ion diffusion is simulated in DFT based molecular dynamics with the activation energy determined as low as 0.27 eV, and the fast Li transport is observed through the wide channels and continued with penetrating movement of Li ions to edge sites. *In-situ* TEM and XRD results show an exclusive intercalation process during lithiation with all the intermediate configurations identified by DFT calculations. The whole intercalation/deintercalation process is determined to proceed *via* a solid solution behavior with continuous lithium (de)occupying/(re)ordering on the identified insertion sites. During the process, no remarkable phase transition is detected with nearly intact host phosphorous niobium oxide backbone. As a result, the fast diffusion channels and insertion cavities are well maintained through cycling, leading to the outstanding rate capacity as observed.

Results and Discussion

Structure and cavity type elucidation for W-R PNb_9O_{25}

Lithium insertion mechanism of W-R phases was first investigated by Cava *et al.*[19] They proposed that insertion mechanism of W-R phases is proceeded *via* occupying the six types (I-VI) of the cavities of the niobium oxide structures (**Figure. 1B(a)**). Then Koçer *et al.* [27] explored the lithium insertion mechanism in three tungsten niobium oxides ($Nb_{12}WO_{33}$, $Nb_{14}W_3O_{44}$, $Nb_{16}W_5O_{55}$) and identified all the window sites to be stable intercalation positions while lattice contractions were observed in the middle of the lithiation. Here in this study, PNb_9O_{25} adopts a ReO_3-derivated structure with partially sheared MO_6 (NbO_6) octahedral arrangement and PO_4 tetrahedra addition. The formed crystallographic shear not only stabilizes the structures against undesirable octahedral distortions of the host framework upon lithiation as observed in ReO_3, but also brings the structure with type III cavities and, in particular, two small cavity types: 1) formed by NbO_6 octahedra and PO_4 tetrahedra (actually 1/4 of type-VI, marked as type-α in this study), 2) formed by four edge-sharing NbO_6 octahedra (marked as type-β in this study) as shown in **Figure. 1B(b)**.

To have a detailed understanding of the intercalation mechanism of PNb_9O_{25}, we need to clarify the interactions between Li and these cavities. To locate the geometric Li-ion intercalation positions in the PNb_9O_{25} structure, various empty sites (**Table. S1** and **Figure. S1**) in the previously defined type-III cavities, type-α cavities and type-β cavities were considered: type-III center and window, type-α center and edge, and type-β center and edge. We define the stable intercalation sites as the sites which generally preserves its geometric positions upon relaxation in the DFT calculations (**Figure. S1**). After a thorough examination of all these sites in the PNb_9O_{25} structure, we find that both the type-III window sites (16 per f.u.) as reported for other W-R phases in previous studies[27] and type-α edge sites (4 per f.u.) are stable upon intercalation.

The potential of one oxide structure on accommodating lithium ions can be estimated by the number of stable insertion sites per unit, which corresponds to the upper limit of its theoretical capacity. Therefore, we counted the numbers of various cavities considered in this study (type I-VI and α, β) for typical W-R phases and also check their potential stable insertion sites with the results summarized in **Table. 1**. The specific information was shown in **Figure. S2**. We make a hypothesis that window sites of all the large cavities (type I-V) are stable insertion sites among all W-R phases considering their similar coordinates which is partially supported by the previous study.[27] Also, all the α edge sites are presumed to be electrochemically active upon thorough lithiations. To make the amount of insertion sites comparable, we also calculated their numbers per electrochemical redox center, which is metal in the compound formula. Among them, PNb_9O_{25}, $Nb_{16}W_5O_{55}$ and $Nb_{18}W_8O_{69}$ have the top amount of stable lithium insertion sites of 2.22, 2.24, 2.31 per metal with the latter two have been reported to be high-rate electrodes.[25,28] Therefore, PNb_9O_{25} show great promises to enable the fast ionic transport and extended intercalation chemistry.

Lithium-ion Storage Examination

To examine the electrochemical performance of PNb_9O_{25}, the PNb_9O_{25} loaded on carbon nanotubes (PNb_9O_{25}@CNTs) were synthesized through a two-step solid-state thermal reaction method and detailed characterizations were performed to reveal the phase/elemental information of the as-synthesized materials (**Figure. S3-S5**). Reaction of PNb_9O_{25}@CNTs with lithium (**Figure. 2A**) proceeds in the potential range from 0.01 to 3.0 V, with an average voltage of 1.47 V, which is lower to the average voltage of $Li_4Ti_5O_{12}$ (1.55 V), $Nb_{18}W_{16}O_{93}$ (1.67 V) and $Nb_{16}W_5O_{55}$ (1.57 V).[25,30] The lower average voltage endows a higher energy density of PNb_9O_{25}@CNTs. The kinetics were examined over a range of current densities from 0.12 C to 48 C (**Figure. 2A, B**). An ultrahigh reversible capacity is achieved with 546 mAh/g based on the total mass of PNb_9O_{25} and CNTs at 0.12 C, which remains 253 mAh/g at 4.8 C and 80 mAh/g at 48 C, indicating the outstanding rate capability of PNb_9O_{25}@CNTs. It should be noted that, the CNTs can significantly improve the electric conductivity and hence enable the thorough charge/discharge of PNb_9O_{25}, meanwhile the interfaces between PNb_9O_{25} and CNTs can also contribute holes/deficiencies to accommodate more Li^+ ions.[31] The composite shows remarkable cycling stability along with a capacity of 203 mAh/g after 1100 cycles under full discharge/charge conditions (0.01-3V) at fixed 7.2 C, demonstrating a capacity retention of 90% (**Figure. 2C, D**). The redox kinetic properties of the PNb_9O_{25}@CNTs was investigated through cyclic voltammetry (CV) experiment at 0.1 mV/s (**Figure. 2E and Figure. S6a**). It is generally believed that the intense cathode /anodic peak pair in the range of 1.5-1.8 V can be attributed to the Nb^{4+}/Nb^{5+} redox couple; and the broad peak pair below 1.5 V can be assigned to the Nb^{3+}/Nb^{4+} redox couple.[32,33]. Simultaneously, similar CV curves of PNb_9O_{25}@CNTs among fresh PNb_9O_{25}@CNTs, after cycling 100 cycles and 200 cycles at 0.24 C further demonstrate excellent structural stability

(**Figure. S6b**). The electrochemical performance of pure PNb_9O_{25} was also tested and shown in **Figure. S7**.

Lithiation Mechanism probed by DFT calculations and In-situ TEM Observation

We conducted a DFT calculation study to investigate the lithium accommodation mechanism of PNb_9O_{25} during the electrochemical lithiation process. We identify the structures of the intermediate configurations by energetically examining all geometrically distinct Li/vacancy orderings on stable intercalation sites as determined in the previous section using an in-house code (**Figure. S8**).[34-36] A number of intercalated intermediate phases are identified on the calculated Li-PNb_9O_{25} convex hull as shown in **Figure. 3A** and **Figure. S9A**. Upon lithiation, the Li-ions first energetically prefer to occupy the type-III window sites until they are completely filled up (x = 16, $Li_xPNb_9O_{25}$); further Li-ion insertion would occupy the type-α edge sites until all the sites are taken (x = 20, $Li_xPNb_9O_{25}$). We plot the discharge voltage profile overlaid with the experimental measurement (**Figure. 3B**), which shows great agreement. During the intercalation process, the system exhibits very limited volume expansion (~14%, **Figure. S9C**.) with a well-preserved PNb_9O_{25} framework (**Figure. 3A**), indicating the excellent cyclability as observed in the experimental observations. It is also noteworthy that, lattice contractions during lithiation along certain directions (a, b in PNb_9O_{25}) previously reported[27] is also observed in this study (**Figure. S10**), indicating their potential existence for all W-R phase. The lithiation of PNb_9O_{25} is then proven to be a complete solid-solution type intercalation process with the continuous Li-ion occupying /reordering which therefore enables its superb cycling performance. Valence variations of P and Nb ions during the lithiation process of PNb_9O_{25} are evaluated using Bader charge analysis.[37] Results indicate a thorough reduction of $Nb^{5+}\rightarrow Nb^{3+}$ during $0 < x < 20$ and the reduction of $P^{5+}\rightarrow P^{3+}$ occurs at the end of the lithiation (x > 16), when Li-ions start to occupy the type-α vacancies, close to the P ions (**Figure. 3A, Figure. S11).** The redox process is further confirmed by the *ex-situ* XPS and XAS observations which show that shifting to the lower binding energy of Nb 3*d* and P 2*p* indicates both Nb and P participate in the electrochemical during the lithiation process (**Figure. S12, 13**).

The lithium intercalation mechanism and the correlation between structural and electrochemical properties in PNb_9O_{25} was further investigated *via* an *in-situ* transmission electron microscopy (TEM) approach, realizing a real-time imaging characterization of the electrochemical process. **Figure. 4A** shows the high-resolution transmission electron microscopy (HRTEM) screen images along the [001] zone-axis direction from **Video S1** as a function of reaction time. **Figure. 4B** shows the local structure evolution of the same area marked by the white rectangle in panel during lithiation process, and the crystallographic planes of (-110) and (110) are labeled. When the time increasing intercalated Li content increased, the (-110) and (110) *d*-spacing increased from the 11.15 Å to 11.35 Å, and 11.06 Å to 11.36 Å, respectively. The combination of HREM and DFT calculation has been proven to be effective in identifying the content of the Li in the intermediate phases.[38] The HREM image from 19s, 25s and 249s matches very well with the structural models generated by DFT calculation with Li lithiation content (x) equals to 2, 3, and 20 respectively (**Figure. 4C**). The PNb_9O_{25} lattice slightly expands and keeps single crystal structure due to open ion transfer channels based on the larger block size, and system exhibits very limited volume expansion (~16.5%, **Figure. 4, S14-16**) suggesting the excellent structural stability as observed in the experimental observations and agrees with the DFT simulated results (~14%). The crystalline phase evolution of PNb_9O_{25} during lithiation is also monitored by the selected area electron diffraction (SAED) pattern along the [1-11] (**Figure. S17**), which indicates that the single-crystal PNb_9O_{25} expands along the (-1-10) and (0-1-1) during the lithiation process. It is worth noting that lithium ion intercalation reaction occurs and results in high density of defects inside of the observed structure, indicated by the appearance of diffraction streaks in **Figure. S17b**. The planar defects are induced by the large in-plane misfit stresses due to lithiation, providing a facile pathway for diffusion, and facilitating lithium ion insertion into the electrode materials.[39-41] Additionally, theoretical calculations show the defects can decrease the lithium ion migration barriers and increase the diffusion coefficients and enhance the energy storage capacity of the electrode.[38,42]

To examine the structural stability of PNb_9O_{25} after cycling, *ex-situ* XRD, *ex-situ* TEM analysis were also carried out. **Figure. 4D** shows the comparison of XRD patterns of PNb_9O_{25}@CNTs at various states: the origin sample, the fully charged (3 V) and fully discharged (0.01 V) sample at the 2nd cycle@ 0.12C, and the 200th cycle at 2.4 C. It is found that, with fully discharging to 0.01 V, the planes of (101), (231), (141) and (521) shifted to low-angle direction, suggesting that these crystal planes are sensitive to the lithiation process; and these peaks return to the original positions after full charging to 3.0 V, suggesting the excellent reversibility during lithiation/delithiation process. This trend is also observed from the XRD patterns of the sample after 200 cycles, which further confirms the excellent structural stability upon charge/discharge cycling. Promisingly, the simulated XRD patterns show exact peaks and shifts as observed experimentally, confirmed the configurations predicted using DFT calculations. Note that, except for peak shift, no new XRD peaks were generated during the lithiation/delithiation process, indicating the solid-solution characteristics of the electrochemical reaction. *Ex-situ* TEM (**Figure. S18,19**) results indicate that, the PNb_9O_{25} remains the homogeneous element distribution and the original single crystal structure after cycling 100 cycles at 0.24 C, further providing clear evidence for the excellent structural stability of the PNb_9O_{25}.

In order to have a mechanistic understanding of the Li kinetics in PNb_9O_{25}, we also performed first-principle molecular dynamic (MD) calculations at different temperatures and the activation energy is calculated by fitting the Arrhenius plot (**Figure. 5A，B**). An essentially small activation energy of 0.27 eV is determined for PNb_9O_{25} which is lower than the well-known fast electrode such as $Li_4Ti_5O_{12}$ (0.3 eV),[43] indicating an excellent Li-ion conductivity and rate capacity of PNb_9O_{25} as observed in this and previous studies.[44] From the recorded Li trajectories, we clearly can see the fast Li transport through the large type-III channel and the penetrating movement of Li ions from the type-III channel to the type-α edge sites (**Figure. 5A, B**). Galvanostatic intermittent titration technique (GITT) analysis was conducted for both the Li insertion and extraction processes of it. The observed GITT curves for insertion Li ions and extraction. Specific information was shown in the **Figure. S20**. Li ion diffusion coefficients (at 298K) for the insertion and extraction are measured to be ($2.77\times10^{-12} m^2/s$) and ($1.62\times10^{-12} m^2/s$), which are higher than the record-high rate electrode of $Nb_{16}W_5O_{55}$ ($2.1\times10^{-12} m^2/s$),[25] confirming the fast Li kinetics in PNb_9O_{25}.The Li^+ diffusion coefficients obtained from the MD simulations ($4.8\times10^{-12} m^2/s$ at 298K) are in great agreement with the GITT measurements (**Figure. 5C, D**). Therefore, it can be summarized that the whole (de)lithiation process exhibits solid-solution reaction features and lithium (de)occupies/(re)orders on the identified insertion sites continuously. Nearly “zero-stress” characteristics is observed with PNb_9O_{25} frameworks almost intact and all the fast diffusion channels and insertion cavities well-maintained upon cycling. The remarkable rate performance and large capacity of PNb_9O_{25} then can be attributed to the robust structure and extensive intercalation chemistry.

Full-Cell construction

To further envisage the practical application potential of our PNb_9O_{25}@CNTs electrode, a full cell battery with a structure of PNb_9O_{25}@CNTs|| 1M $LiPF_6$/EC (ethylene carbonate) +DMC (dimethyl carbonate) || NCM was assembled within the potential range from 1.3-4.3V (**Figure. 6A**). The PNb_9O_{25}@CNTs anode was electrochemically pre-activated for lithium ions intercalation. In order to rationally analyze the electrochemical performance, the mass ratio of the cathode and anode materials was decided as 2.6:1 for charge balance (**Figure. 6B**). The galvanostatic charge-discharge profiles of full cell at 0.4 C are presented in the **Figure. 6C**. The sloping potential plateaus at *ca*. 3.8 V are observed for all the three charge -discharge process, with the discharge capacity approaching 372 mAh/g due to the lower average voltage. **Figure. 6D** demonstrates the excellent rate performance of the full cell with specific capacity of 372 mAh/g and 59 mAh/g at 0.4 C and 24 C, respectively based on anode mass. The Ragone plot as illustrated in **Figure. 6E** demonstrates the highest energy density of 333.5 Wh kg^{-1} based on total mass of both electrodes (1202 Wh/kg based on the anode mass, **Figure. S21**) with a power density of 156.2 W/kg. Even if the current rate increases up to 16 C, the energy density remains 79.6 Wh/kg with the corresponding power density as high as 5277.35 W/kg. Our maximum energy density and the corresponding power density is much higher than previously reported LIB full cell devices of FCG//Si/C-IWGS (360 Wh/kg at 72 W/kg),[45] LCO/TO-MO (285 Wh/kg at 136 W/kg),[46] ZFO-600//LFP-CNT (202 Wh/kg at 75 W/kg),[47] LMO//TiO_2 (148.8 Wh/kg at 148.8 W/kg),[48] LNMO//MnO (286.5 Wh/kg at 14.3 W/kg),[49] LMO//SnO_2 (124.7 Wh/kg at 79.6 W/kg),[50] LCP//LTO (218.6Wh/kg at 21.9 W/kg),[51] LFP//TiO_2 (103 Wh/kg at 34.3 W/kg),[52] (**Figure. 6E**). The higher energy density and power density of PNb_9O_{25}@CNTs can be contributed to following aspects. On the one hand, the lower average voltage (~1.47 V) of PNb_9O_{25} endows the full cell with higher output voltage; on the other hand, the larger block size provides open channels and a large amount of lithium insertion sites which can accelerate Li ion transportation and ensure the system with large capacity.

Conclusions

In summary, we survey all the known W-R structures and we are able to construct a connection between the cavity number of a structure and its capability upon accommodating lithium ions for the first time. Based on this principle, we identify two geometrical types of stable insertion sites in PNb_9O_{25} structure with the total amount (20 per f.u., 2.22 per Nb ion) and a measured remarkable high reversible capacity of 546 mAh/g. We also observe a remarkable cycling stability (90% capacity retention after 1100 cycles at 7.2C) of PNb_9O_{25}@CNTs under full lithiation/delithiation conditions (0.01-3V). Further, we have revealed the intercalation mechanism of W-R phase PNb_9O_{25} by combining *in-situ* TEM, *ex-situ* XRD and DFT calculations, and unveil the origin of the promising structural stability. The lithiation process of PNb_9O_{25} was simulated with DFT calculation and MD, which identifies 20 insertion sites per formula unit (f.u.) showing a very low activation energy of 0.27 eV, and the discharge voltage profile is in good agreement with the experimental measurement. The whole intercalation/deintercalation process is determined to proceed *via* a solid solution behavior with continuous lithium (de)occupying/(re)ordering on the identified insertion sites. *In(ex)-situ* TEM and *ex-situ* XRD results demonstrate the exclusive intercalation process during lithiation, the intermediate during charging or final structures after cycles also corresponds well with the DFT simulated configurations. Simultaneously, PNb_9O_{25} exhibits very limited volume expansion < 16.5%. A full-cell lithium ion battery has been constructed exhibiting a very high energy density of 1202 Wh/kg based on the mass of anode material, which can be attributed to the appropriate average voltage (~1.47 V) and open channels in PNb_9O_{25}.

Methods

Chemicals. Niobium(V) chloride ($NbCl_5$) was purchased from Aladdin (99%, CAS:10026-12-7). Ethylene glycol (EG) was purchased from the Aladdin (AR, 98%, CAS:107-21-1). Red phosphorous was purchased from the Aladdin (AR, 98.5%, CAS:7723-14-0). The Multi-wall carbon nanotubes (MWCNTs) were purchased from XFNANO (D＜8 nm×L 0.5-2 um,＞95%),

Preparation of materials

PNb_9O_{25}/SWCNTs composites were prepared by a facile solvothermal reaction.

Synthesis of precursor of PNb_9O_{25}@CNTs: In a typical synthesis procedure, 0.075 g CNTs were dispersed in 30 mL of ethylene glycol (EG) and stirred for 1 h. Furthermore, 0.25 g $NbCl_5$ were dissolved in the 30 mL of ethylene glycol (EG) with magnetic stirring for 30 min, giving rising to a homogeneous solution. Subsequently, the two solutions were mixed under magnetic stirring for 30 min. Finally, the obtained solution was transferred into a 100 mL Teflon container, sealed in an autoclave, and hydrothermally reacted at 180°C for 24 h. The as-synthesized product was adequately washed several times with deionized water and alcohol, respectively, and further collected by centrifugation. The obtained precursor was allowed to dry in a nitrogen stream.

Synthesis of PNb_9O_{25}/CNTs Composites: For the preparation of PNb_9O_{25}/CNTs composite, precursor and red P with a weight ratio of 1:3 was hand-milled in a mortar for 15 min. Subsequently, the mixture was further annealed at 900ºC in an Ar flow for 3 h with a ramping rate of 2°C min^{-1} to obtain the targeting material.

The pure PNb_9O_{25} has a similar synthetic method without adding the CNTs.

Material characterizations

Powder X-ray diffraction (XRD) patterns between 10 and 80° (~2θ) were collected by Rangaku D/MAX-2500 powder diffractometer with Cu−Kα radiation (λ=0.154 nm) operated at 40 kV, 200 mA. Hitachi-X-ray photoelectron spectrum (XPS) was measured by a VG ESCALAB MKIIX-ray photoelectron spectrometer using Mg−Kα as the exciting source (1253.6 eV). TG measurement was carried out by using Netzsch STA 449C thermal analyzer. Carl Zeiss SUPRA 55 SAPPHIRE field emission scanning electron microscope (FESEM, Germany, 15 kV) Hitachi-7650 transmission electron microscopy (TEM, Japan, 80 kV), and high-resolution transmission electron microscopy (HRTEM, JEOL JEM-3000F) were used to investigate the morphology and microstructure.

Electrochemical studies

The working electrodes were prepared by mixture of 80 wt% synthesized active materials, 10 wt% acetylene carbon black, 10 wt% PVDF binder in N-methyl-2-pyrrolidone (NMP) onto a Cu foil and then dried in a vacuum furnace at 120 °C for 12 h. The 25 μm microporous monolayer membrane (PP, Celgard 2400) and Li metal was used as separator and counter electrodes respectively when assembled into a stainless-steel coin cell (2032) in an Ar-filled glovebox (both O_2 and H_2O levels below 0.1 ppm). The electrochemical measurements were tested in 1 M $LiPF_6$ solution in a mixture (1:1:1, in vol%) of dimethyl carbonate (DMC), ethylene carbonate (EC), and ethylmethyl carbonate (EMC) for LIBs. Cyclic voltammetry (CV) curves were tested on CHI650e electrochemical workstation (Chenhua, China) with the scanning rate of 0.1 mV s^{-1}. The constant current charge-discharge tests were performed with a computer-controlled cycling equipment (Land CT2001A, China) in the potential rage of 0.01~3V. PNb_9O_{25}@CNTs and commercial $LiNi_xCo_yMn_{1-x-y}O_2$ (333) were used as anode material and cathode material of full cell, respectively. The energy density (E) and power density (P) of full cell were calculated according to the following equations:

$$E = \int_{t1}^{t2} IV_{(t)}dt \qquad (1)$$

$$P = \frac{\mathrm{E}}{\mathrm{t}} \qquad (2)$$

I is the current, V is the discharge voltage, *t* is the discharge time.

First-principle calculations

All the first-principles calculations were performed *via* the Vienna Ab-initio Simulation Package (VASP)[53-56] within the projector augmented wave (PAW) formalism[57] and the Perdew-Becke-Ernzerhof (PBE) approximation[58] to the exchange-correlation potential was employed. We used a plane wave basis with a cutoff energy of 520 eV and **Γ**-centered *k*-meshes with a density of 8000 *k*-points per reciprocal atom. We search the intermediate intercalated phases through the Li-PNb_9O_{25} reaction using the Non-Equilibrium Phase Search method (NEPS)[34-36] by exploring geometrically distinct Li/vacancy configurations on the stable insertion sites of the PNb_9O_{25} structure (**Figure 1**) at different compositions (Li/vacancy ratios). The method proceeded as follows: i) identify all possible stable insertion sites in the original PNb_9O_{25} structure; ii) generate all symmetrically distinct configurations with Enum[59,60] for a series of compositions $Li_x\square_{3-x}PNb_9O_{25}$ ($0 < x < 20$, □ denoting vacancy); iii) sample electrostatic total energies of all configurations; iv) rank the structures by the total energies for each specific stoichiometry, and calculate the formation energies by relaxing three lowest energy structures with accurate settings according to the reaction $PNb_9O_{25} + x\mathrm{Li} \rightarrow \mathrm{Li}_xPNb_9O_{25}$; v) construct the lithiation convex hull using the formation energies and determine the composition points on the hull as the intermediate phases. The average lithiation voltage (relative to $\mathrm{Li/Li^+}$) was computed using the negative of the reaction free energy per Li added following the ground state convex hull (T = 0K) to form a series of constant voltage steps along the two-phase regions of the convex hull, which should be viewed as an approximation to the actual voltage profiles. At elevated temperatures (*e.g.*, room temperature), the abrupt voltage drops become more rounded, due to entropic effects, which would be smoother when finite temperature effects are included.[61] To evaluate the Li-ion conductivity of PNb_9O_{25}, we created a 1×1×2 supercell and simulated the canonical (NVT) ensemble through a Nosé thermostat with a minimal Γ-centered 1×1×1 k-point grid.[62] In each run, velocity−Verlet was used for a time integration scheme with a step of 2 fs. Considering thermal expansion, we conducted a series of volume-varying picosecond runs at each target temperature. Therefore, the volume of the supercell was determined, where the average pressure was approximately zero. When the MD simulations started, the Li-PNb_9O_{25} systems were assigned an initial temperature of 100 K, and it was heated to target temperatures (600K - 1800 K) in 2 ps and equilibrated for 5 ps. We performed MD simulations to conduct the diffusion for 40 ps. In addition, Li-ion diffusivities at each target temperature were calculated by fitting the mean square displacement over time using the following equation: $\mathrm{D} = \frac{1}{2t}[r(t)]^2$. Here, $r(t)$ is the displacement of ions at time t and D was obtained by a linear fitting to the dependence of average mean square displacement over $2t$.

***In situ* TEM characterization**

Taking the advantage of the nanobattery setup reported in the previous articles.[63-68] The nanobattery system was built on the X-Nano TEM holder, which was developed by the Center for X-Mechanics, Zhejiang University. It consists a compact four-degree freedom (positioning in X, Y, Z-directions plus self-rotation) nano-manipulator and in-situ electrical biasing function. The PNb_9O_{25} nanoparticles were loaded on the one side of the holder as working electrode, Li/Li_2O was scratched on the other side of the X-Nano TEM holder, served as the counter electrode and the solid electrolyte. The probe moving resolution can be accurately controlled by less than 1 nm. When the two electrodes contacted together, one negative bias was applied to drive the lithium ion insertion. While for the lithium extraction, a positive bias needed to be applied between these two electrodes.

Data and materials availability: All data needed to evaluate the conclusions in the paper are present in the paper and/or the Supplementary Materials. Additional data related to this paper may be requested from the authors.

References:

1. Goodenough, J. B. & Park, K. S. The Li-ion rechargeable battery: A perspective. *J. Am. Chem. Soc.* **135**, 1167-1176 (2013).
2. Cano, Z. P. et al. Batteries and fuel cells for emerging electric vehicle markets. *Nat. Energy* **3**, 279-289 (2018).
3. Harper, G. et al. Recycling lithium-ion batteries from electric vehicles. *Nature* **575**, 75-86 (2019).
4. Liu, Y., Zhu, Y. & Cui, Y. Challenges and opportunities towards fast-charging battery materials. *Nat. Energy* **4**, 540–550 (2019)

5. Yu, Y. et al. Achieving High-energy full-cell lithium-storage performance by coupling high-capacity V_2O_3 with low-potential Ni_2P anode. *ACS Appl. Mater. Interfaces.* **11**, 19-25 (2019).
6. Mizushima, K., Jones, P. C., Wiseman, P. J. & Goodenough, J. B. $LixCoO_2$ ($0<x<1$):A new cathode material for batteries of high energy density. *Mater. Res. Bull.* **15**, 783–789 (1980).
7. Padhi, A. K., Nanjundaswamy, K. S. & Goodenough, J. B. Phospho-olivines as positive-electrode materials for rechargeable lithium batteries. *J. Electrochem. Soc.* **144**, 1188–1194 (1997).
8. Ohzuku, T. & Makimura, Y. Layered lithium insertion material of $LiCo_{1/3}Ni_{1/3}Mn_{1/3}O_2$ for lithium-ion batteries. *Chem. Lett.* **30**, 642–643 (2001).
9. Perez, A. J. et al. Approaching the limits of cationic and anionic electrochemical activity with the Li-rich layered rocksalt Li_3IrO_4. *Nat. Energy*. **2**, 954–962 (2017).
10. Lee, J. et al. Reversible Mn^{2+}/Mn^{4+} double redox in lithium-excess cathode materials. *Nature* **556**, 185–190 (2018).
11. Chan, C. K. et al. High-performance lithium battery anodes using silicon nanowires. *Nat. Nanotechnol.* **3**, 31–35 (2008).
12. Huang, S. et al. N-graphene motivated $SnO_2@SnS_2$ heterostructure quantum dots for high performance lithium/sodium storage. *Energy Storage Mater* **20**, 225-233 (2019).
13. Shi, S. et al. A covalent heterostructure of monodisperse Ni_2P immobilized on N, P-co-doped carbon nanosheets for high performance sodium/lithium storage. *Nano Energy* **48**, 510-517 (2018).
14. Vetter, J. et al. Ageing mechanisms in lithium-ion batteries. *J. Power Sources* **147**, 269–281 (2005).

15. Fang, R. et al. The regulating role of carbon nanotubes and graphene in lithium-ion and lithium-sulfur batteries. *Adv. Mater.* **31**, 1800863 (2019).

16. Downie, L. E. et al. In situ detection of lithium plating on graphite electrodes by electrochemical calorimetry. *J. Electrochem. Soc*. **160**, A588–A594 (2013).

17. Jansen, A. et al. Development of a high-power lithium-ion battery. *J. Power Sources* **81/82**, 902–905 (1999).

18. Odziomek, M. et al. Hierarchically structured lithium titanate for ultrafast charging in long-life high capacity batteries. *Nat. Commun*. **8**, 15636 (2017).

19. Cava, R. J., Murphy, D. W. & Zahurak, S. M. Lithium insertion in Wadsley-Roth phases based on niobium oxide. *J. Electrochem. Soc*. **130**, 2345–2351 (1983).

20. Augustyn, V. et al. High-rate electrochemical energy storage through Li^+ intercalation pseudocapacitance. *Nat. Mater*. **12**, 518–522 (2013).

21. Griffith, K. J., Forse, A. C., Griffin, J. M. & Grey, C. P. High-rate intercalation without nanostructuring in metastable Nb_2O_5 bronze phases. *J. Am. Chem. Soc*. **138**, 8888–8899 (2016).

22. Han, J.-T., Huang, Y.-H. & Goodenough, J. B. New anode framework for rechargeable lithium batteries. *Chem. Mater*. **23**, 2027–2029 (2011).

23. Griffith, K. J. *et al.* Ionic and electronic conduction in $TiNb_2O_7$. *J. Am. Chem. Soc*. **141**, 16706-16725 (2019).

24. Saritha, D., Pralong, V., Varadaraju, U. V. & Raveau, B. Electrochemical Li insertion studies on $WNb_{12}O_{33}$—A shear ReO_3 type structure. *J. Solid State Chem*. **183**, 988–993 (2010).

25. Griffith, K. J., Wiaderek, K. M., Cibin, G., Marbella, L. E. & Grey, C. P. Niobium tungsten oxides

for high-rate lithium-ion energy storage. *Nature* **559**, 556–563 (2018).

26. Patoux, S., Dolle, M., Rousse, G. & Masquelier, C. A reversible lithium intercalation process in an ReO_3-type structure PNb_9O_{25}. *J. Electrochem. Soc.* **149**, A391–A400 (2002).
27. Kocer, C. P., Griffith, K. J., Grey, C. P. & Morris, A. J. Cation disorder and lithium insertion mechanism of Wadsley-Roth crystallographic shear phases from first principles. *J. Am. Chem. Soc.* **141**, 15121-15134 (2019).
28. Griffith, K. J. & Grey, C. P. Superionic Lithium Intercalation through 2 nm× 2 nm Columns in the Crystallographic Shear Phase $Nb_{18}W_8O_{69}$. *Chem Rxiv* (2019).
29. Deng, S., Zhu, H., Wang, G. *et al.* Boosting fast energy storage by synergistic engineering of carbon and deficiency. *Nat Commun* **11,** 132 (2020).
30. Naoi, K., Ishimoto, S., Isobe, Y. & Aoyagi, S. High-rate nano-crystalline $Li_4Ti_5O_{12}$ attached on carbon nano-fibers for hybrid supercapacitors. *J. Power Sources* **195**, 6250-6254 (2010).
31. Chen, C.-C., Fu, L. & Maier, J. Synergistic, ultrafast mass storage and removal in artificial mixed conductors. *Nature* **536**, 159-164 (2016).
32. $Ti_2Nb_{2x}O_{4+5x}$ anode materials for lithium-ion batteries: a comprehensive review. *J. Mater Chem A* **6**, 9799-9815 (2018).
33. Wang, X., Shen, G. Intercalation pseudo-capacitive $TiNb_2O_7$@ carbon electrode for high-performance lithium ion hybrid electrochemical supercapacitors with ultrahigh energy density. *Nano Energy* **15**, 104-115 (2015).
34. Yao, Z. et al. Revealing the conversion mechanism of transition metal oxide electrodes during lithiation from first-principles. *Chem. Mater.* **29**, 9011–9022 (2017).

35. Yao, Z., Kim, S., He, J., Hegde, V. I. & Wolverton, C. A quasi two-dimensional copper–bismuth nanosheet. *Sci. Adv.* **4**, 6754 (2018).

36. Amsler, M., Yao, Z. & Wolverton, C. Cubine, a quasi two-dimensional copper–bismuth nanosheet. *Chem. Mater.* **29**, 9819–9828 (2017).

37. Tang, W., Sanville, E. & Henkelman, G. A. A grid-based bader analysis algorithm without lattice bias. *J. Phys.: Condens. Matter* **21**, 084204 (2009).

38. Li, Q. et al. Intermediate phases in sodium intercalation into MoS_2 nanosheets and their implications for sodium-ion batteries. *Nano Energy* **38**, 342-349 (2017).

39. Nie, A. et al. Atomic-scale observation of lithiation reaction front in nanoscale SnO_2 materials. *ACS Nano* **7**, 6203-6211 (2013).

40. Legros, M., Dehm, G., Arzt, E. & Balk, T. J. Observation of giant diffusivity along dislocation cores. *Science* **319**, 1646-1649 (2008).

41. Nie, A. et al. Twin boundary-assisted lithium ion transport. *Nano Lett* **15**, 610-615 (2015).

42. Panchmatia, P. M., Armstrong, A. R., Bruce, P. G. & Islam, M. S. Lithium-ion diffusion mechanisms in the battery anode material $Li_{(1+x)}V_{(1-x)}O_{(2)}$. *Phys Chem Chem Phys* **16**, 21114-21118 (2014).

43. Ohzuku, T., Ueda, A. & Yamamoto, N. Zero-strain insertion material of $Li[Li_{1/3}Ti_{5/3}]O_4$ for rechargeable lithium cells. *J. Electrochem. Soc.* **142**, 1431–1435 (1995).

44. Drozhzhin, O. A. *et al.* Li-ion diffusion in $Li_xNb_9PO_{25}$. *Electrochim. Acta* **89**, 262–269 (2013).

45. Chae, C., Noh, H. J., Lee, J. K., Scrosati, B. & Sun, Y. K. A high-energy Li-ion battery using a silicon-based anode and a nano-structured layered composite cathode. *Adv. Funct. Mater.* **24**, 3036-

3042 (2014).

46. Wang, C. *et al.* Fabrication and shell optimization of synergistic TiO_2-MoO_3 core–shell nanowire array anode for high energy and power density lithium-ion batteries. *Adv. Funct Mater.* **25**, 3524-3533 (2015).

47. Varzi, A., Bresser, D., Zamory, J., Müller, F. & Passerini, S. $ZnFe_2O_4$-C/$LiFePO_4$-CNT: A novel high-power lithium-ion battery with excellent cycling performance. *Adv. Energy Mater*. **4**, 1400054 (2014).

48. Aravindan, V. *et al.* A novel strategy to construct high performance lithium-ion cells using one dimensional electrospun nanofibers, electrodes and separators. *Nanoscale.* **5**, 10636-10645 (2013).

49. Xu, G.-L. *et al.* Facile synthesis of hierarchical micro/nanostructured MnO material and its excellent lithium storage property and high performance as anode in a MnO/$LiNi_{0.5}Mn_{1.5}O_{4-\delta}$ lithium ion battery. *ACS Appl. Mater. Interfaces*. **5**, 6316-6323 (2013).

50. Park, G. D., Lee, J. K. & Kang, Y. C. Synthesis of uniquely structured SnO_2 hollow nanoplates and their electrochemical properties for Li-ion storage. *Adv. Funct. Mater*. **27**, 1603399 (2017).

51. Ni, J., Liu, W., Liu, J., Gao, L. & Chen, J. Investigation on a 3.2 V $LiCoPO_4$/$Li_4Ti_5O_{12}$ full battery. *Electrochem. Commun*. **35**, 1-4 (2013).

52. Zhang, X. *et al.* Synthesis of TiO_2 hollow nanofibers by co-axial electrospinning and its superior lithium storage capability in full-cell assembly with olivine phosphate. *Nanoscale* **5**, 5973-5980 (2013).

53. Kresse, G. & Hafner, J. Ab initio molecular dynamics for liquid metals. *Phys. Rev*. B **47**, 558–561 (1993).

54. Kresse, G. & Hafner, J. Ab initio molecular-dynamics simulation of the liquid-metal-amorphous-semiconductor transition in germanium. *Phys. Rev.* B **49**, 14251–14269 (1994).

55. Kresse, G. & Furthmüller, J. Efficiency of ab-initio total energy calculations for metals and semiconductors using a plane-wave basis Set. Comput. *Mater. Sci*. **6**, 15–50 (1996).

56. Kresse, G. Efficient iterative schemes for ab initio total-energy calculations using a plane-wave basis set. *Phys. Rev.* B **54**, 11169–11186 (1996).

57. Blöchl, P. E. Projector augmented-wave method. Phys. Rev. B 50, 17953–17979 (1994).

58. Perdew, J. P., Ernzerhof, M. & Burke, K. Rationale for mixing exact exchange with density functional approximations. *J. Chem. Phys*. **105**, 9982–9985 (1996).

59. Hart, G. L. W. & Forcade, R. W. Algorithm for generating derivative structures. *Phys. Rev*. B **77**, 224115–224126 (2008).

60. Hart, G. L. W. & Forcade, R. W. Generating derivative structures from multilattices: algorithm and application to hcp alloys. *Phys. Rev*. B **80**, 014120–014127 (2009).

61. Wolverton, C. & Zunger, A. First-principles prediction of vacancy order-disorder and intercalation battery voltages in $LixCoO_2$. Phys. *Rev. Lett*. **81**, 606–609 (1998).

62. Nosé, S. A unified formulation of the constant temperature molecular dynamics methods. *J. Chem. Phys*. **81**, 511–519 (1984).

63. Liu, X. H. et al. In situ TEM experiments of electrochemical lithiation and delithiation of individual nanostructures. *Adv. Energy Mater*. **2**, 722-741 (2012).

64. Huang, J. Y. et al. In situ observation of the electrochemical lithiation of a single SnO_2 nanowire electrode. *Science* **330**, 1515-1520 (2010).

65. Liu, X. H. et al. In situ atomic-scale imaging of electrochemical lithiation in silicon. *Nat. Nanotechnol.* **7**, 749 (2012).

66. Wang, C.-M. et al. In situ TEM investigation of congruent phase transition and structural evolution of nanostructured silicon/carbon anode for lithium ion batteries. *Nano Lett* **12**, 1624-1632 (2012).

67. Yuan, Y. et al. Asynchronous crystal cell expansion during lithiation of K^+-stabilized α-MnO_2. *Nano Lett* **15**, 2998-3007 (2015).

68. He, K. *et al.* Visualizing non-equilibrium lithiation of spinel oxide via in situ transmission electron microscopy. *Nature Commun.* **7**, 11441 (2016).

Acknowledgement

Funding: The National Natural Science Foundation of China (51774251), Hebei Natural Science Foundation for Distinguished Young Scholars (B2017203313), Hundred Excellent Innovative Talents Support Program in Hebei Province (SLRC2017057), Scientific Research Foundation for the Returned Overseas Chinese Scholars (CG2014003002). Computations were performed on the niagara supercomputer at the SciNet HPC Consortium. SciNet is funded by: the Canada Foundation for Innovation; the Government of Ontario; Ontario Research Fund - Research Excellence; and the University of Toronto. The *in situ* TEM experiments was supported by the National Natural Science Foundation of China (Grant No. 51702207 and 11972219), and the Program for Professor of Special Appointment (Young Eastern Scholar Program) at Shanghai Institutions of Higher Learning. We also want to express our great gratitude for Prof. Bruce Dunn from University of California, Los Angeles (UCLA), and Prof. Wenwen from Shanghai Synchrotron Light Source, for their professional insights and kind support during the preparation of the manuscript.

Author contributions: Y. Zhao supervised the project. Y. Zhao and Z. Yao conceived the project. W. Miao and J. Zhang performed most of the experiments and analyzed the experimental data. Z. Yao conducted DFT calculation on determining the lithium ion intercalation sites, exploring the electrochemical lithiation, and evaluating the ionic mass transport. Q. Li performed the *in situ* TEM and interpretation. Y. Zhao, J. Zhang and A. Aspuru-Guzik provided overall direction and advice for the project. All of the authors contributed to the writing to the manuscript before submission. M. Wang, Z. Yao, and Q. Li contributed equally to the project.

Competing interests: All authors declare that they have no competing interests.

Tables

Tab. 1 | Comparison of the cavity types and stable insertion site numbers among Wadsley-Roth phases.

M represents transition metals in the compound formula.

Compound	Cavity type, and number per unit cell								Total insertion sites	
	I	II	III	IV	V	VI	α (1/4VI)	β	per cell	Per M
This work	**0**	**0**	**8**	**0**	**0**	**0**	**8**	**4**	**40**	**2.22**
$Nb_{18}W_8O_{69}$[28]	8	16	8	0	0	0	8	12	120	2.31
$Nb_{16}W_5O_{55}$[25]	4	12	8	0	0	0	8	10	94	2.24
$Nb_{14}W_3O_{44}$	2	8	8	0	0	0	8	8	74	2.18
$TiNb_2O_7$	0	0	0	4	4	0	0	6	32	2.13
$WNb_{12}O_{33}$	0	2	4	0	0	0	4	3	27	2.08
$MoNb_{12}O_{33}$	0	2	4	0	0	0	4	3	27	2.08
N-Nb_2O_5	2	8	0	4	4	0	0	10	66	2.06
$TiNb_{24}O_{62}$	0	8	8	4	4	0	8	14	100	2.00
VNb_9O_{25}	0	0	8	0	0	2	8	4	40	2.00
$ZrNb_{24}O_{62}$	0	8	8	4	4	0	8	14	100	2.00
$Ti_2Nb_{10}O_{29}$[29]	0	8	0	8	8	0	0	16	92	1.92

Figures

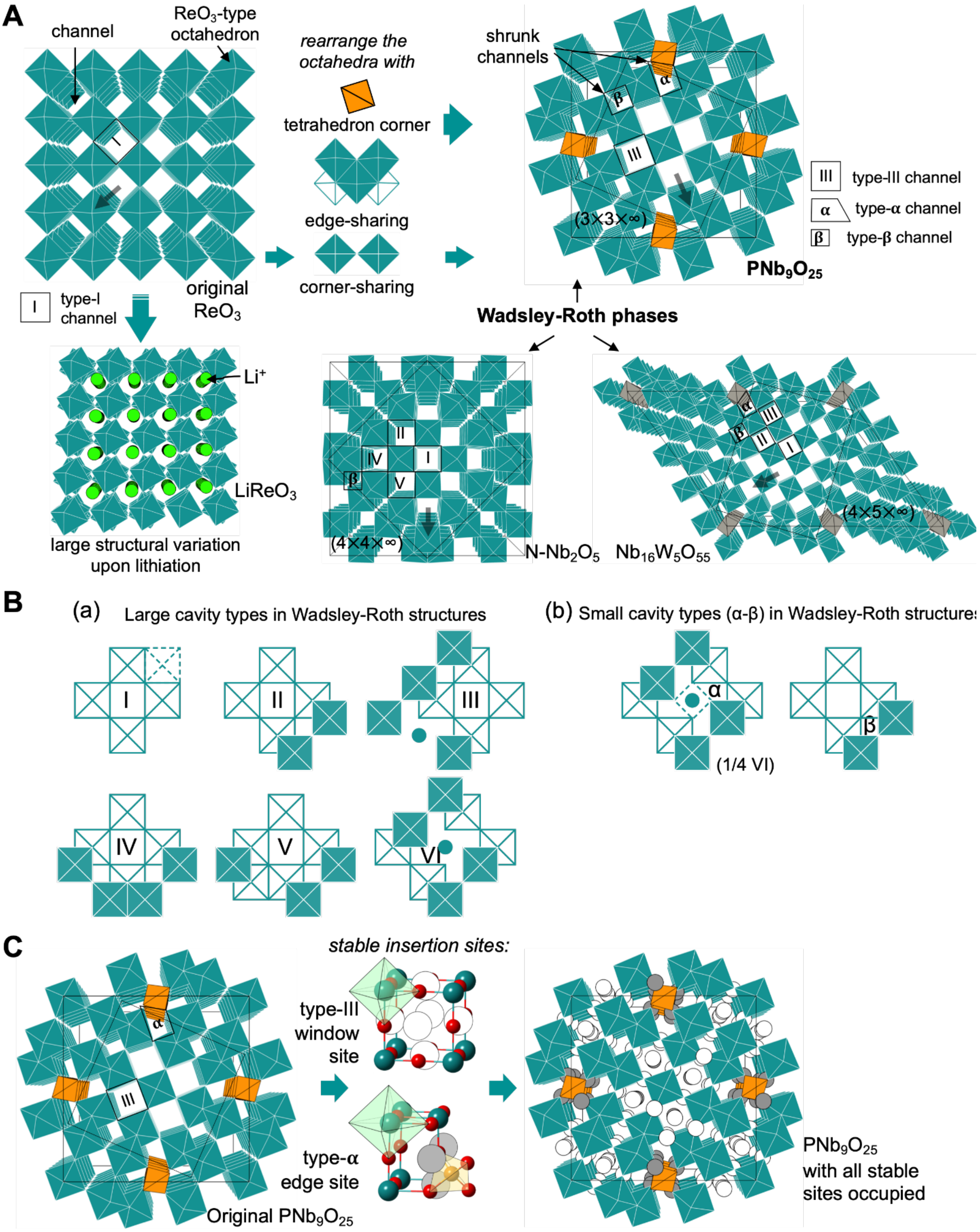

Fig. 1 | Structure evolution of the Wadsley-Roth phases and their intercalation chemistry. A, Structural evolution from standard ReO$_3$ structure to PNb$_9$O$_{25}$ structure and typical Wadsley-Roth phases. B, (a) The six large cavity types (I-VI) in Wadsley-Roth structures. (b) Two small cavity types (α and β) in Wadsley-Roth phases defined in this study. C, Identified stable insertion sites in the PNb$_9$O$_{25}$ structure.

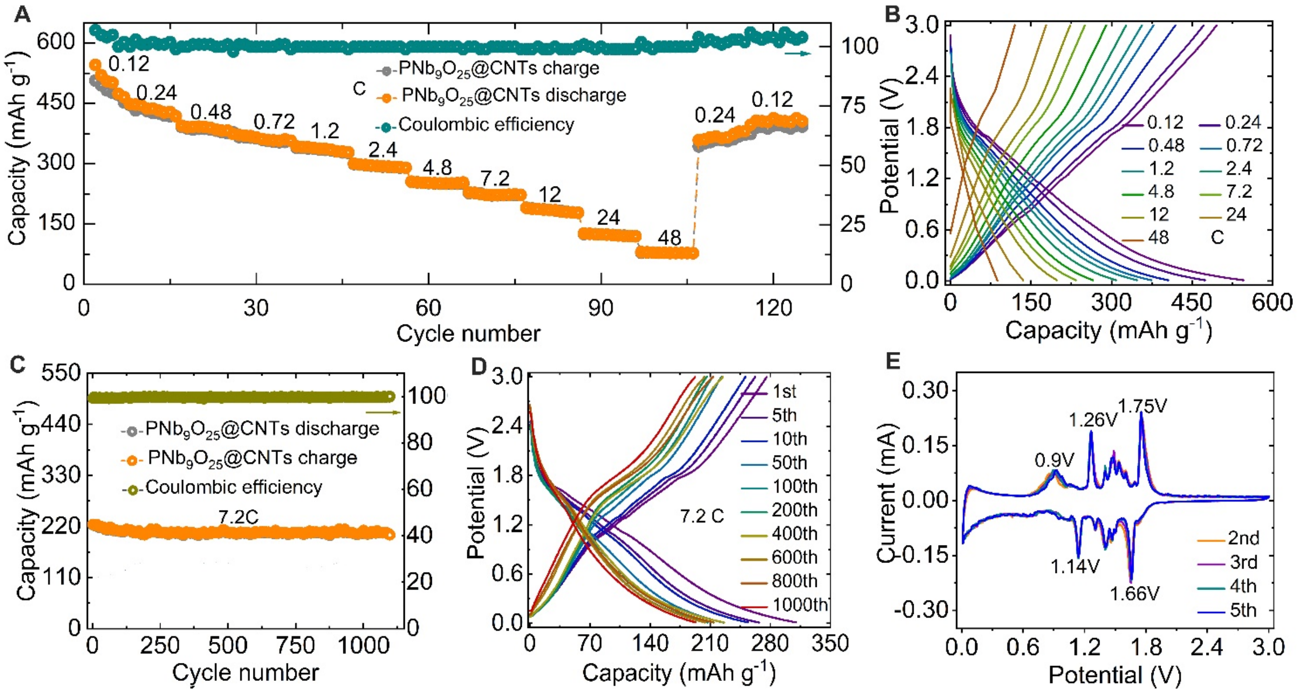

Fig. 2 | Electrochemistry of PNb$_9$O$_{25}$@CNTs. A, Rate performance of PNb$_9$O$_{25}$@CNTs based on gravimetric capacity. B, Galvanostatic discharge and charge curves of PNb$_9$O$_{25}$@CNTs at various density. C, High-rate cycling of PNb$_9$O$_{25}$@CNT. D, Galvanostatic discharge and charge curves of PNb$_9$O$_{25}$@CNTs at 7.2 C. E, Cyclic voltammogram curves of PNb$_9$O$_{25}$@CNTs at 0.1 mV/s.

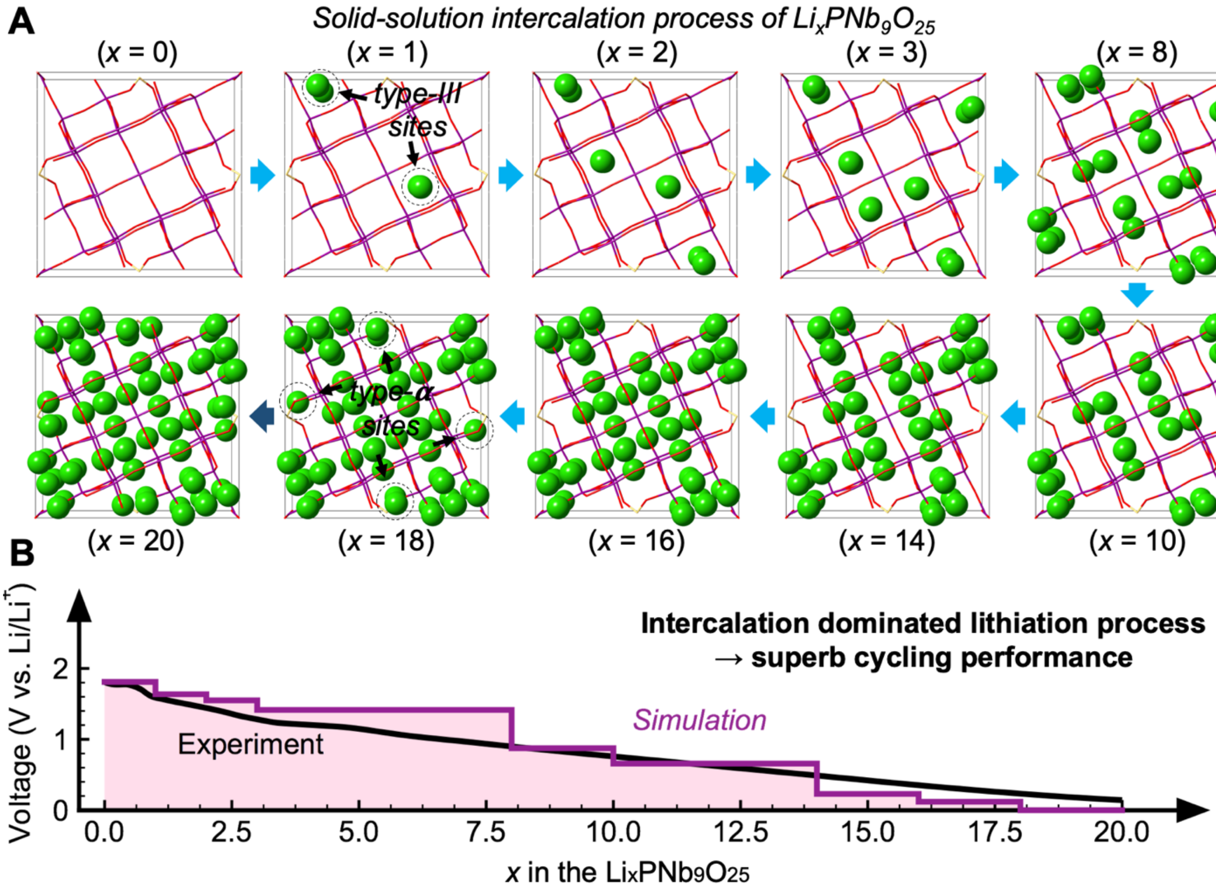

Fig. 3 | Electrochemical lithiation process of the PNb_9O_{25}. A, Predicted structures of the intermediate phase during the electrochemical lithiation (PNb_9O_{25} structure is shown using a stick model to ease the visualization of the Li-ion configuration evolution) and B, the corresponding voltage profile obtained from our calculation, matches the experimental voltage curve.

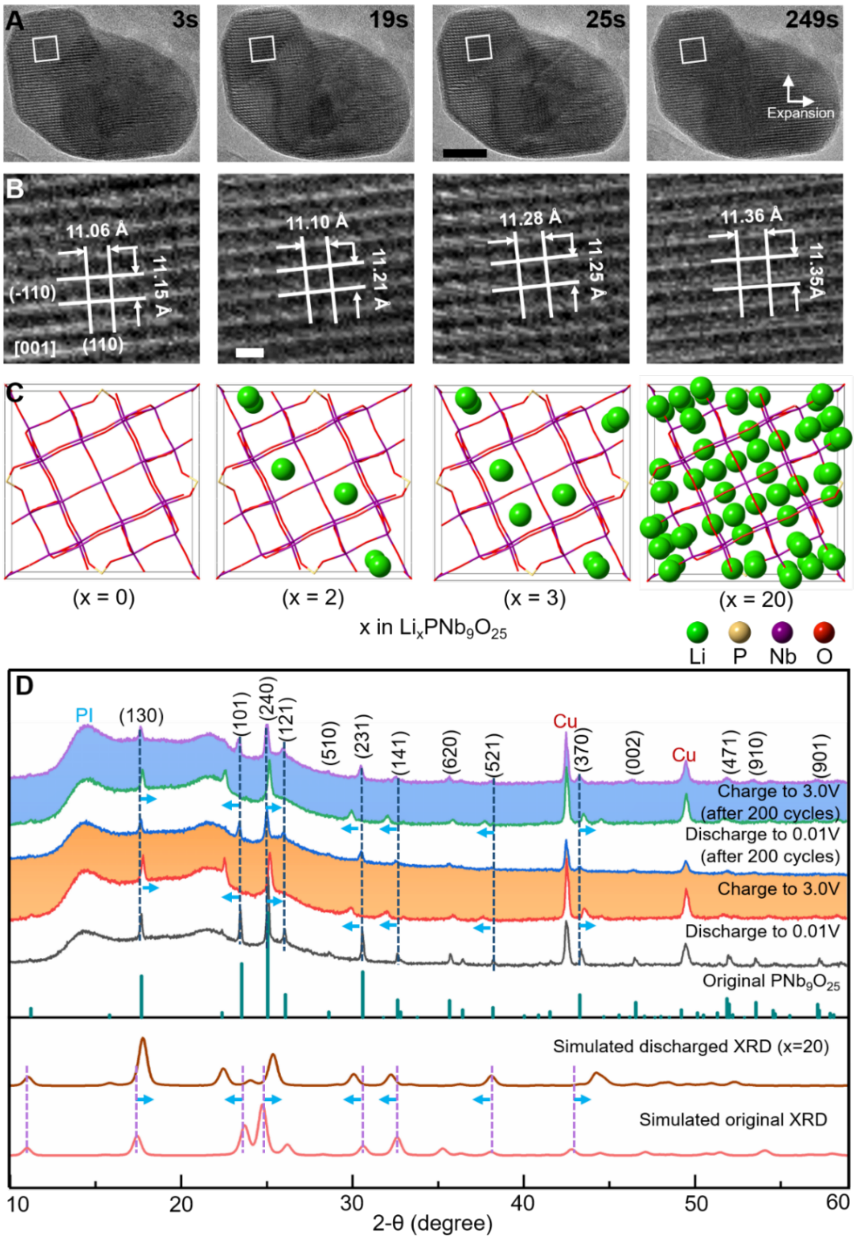

Fig. 4 | In-situ and ex-situ characterization of robust PNb$_9$O$_{25}$ framework (the scale bar is 1 nm)**.** A, *In-situ* TEM lithiation of PNb$_9$O$_{25}$ nanoparticle at relatively low lithiation speed and HRTEM images of the lithiation process as a function of time (seconds). B, Local structural evolution with *d*-spacing changing of {110} during lithiation process. C, Structural models of lithium-inserted phases, from PNb$_9$O$_{25}$ to Li$_x$PNb$_9$O$_{25}$ (x = 2, 3, 20), predicted by DFT simulations. The structural model is oriented along the same direction as the [001] PNb$_9$O$_{25}$. D, *Ex*-situ XRD of PNb$_9$O$_{25}$ electrode with discharging to 0.01 V and charging to 3.0 V after cycling 2 cycles at 0.12 C and cycling the 200 cycles at 2.4 C was measured.

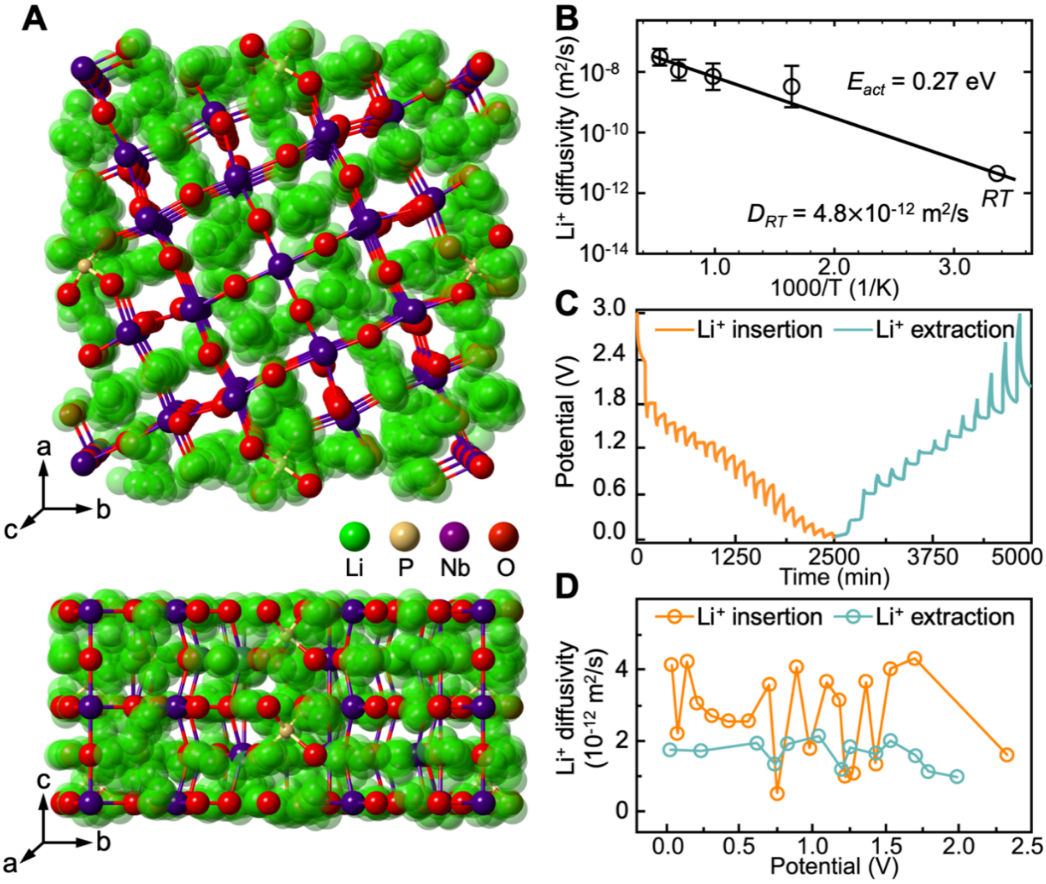

Fig. 5 | Determination of the Li diffusion in the PNb_9O_{25} W-R structure. A, Li-ion diffusion trajectory cloud (green) in the PNb_9O_{25} structure. B, Arrhenius plot of the overall Li-ion diffusion coefficient. C, GITT Li^+ insertion -extraction curves *versus* test time (min) of PNb_9O_{25} tested in the first cycle at 0.1 C. D, Li^+ diffusion coefficient (D_{Li}) of PNb_9O_{25} calculated from GITT curves.

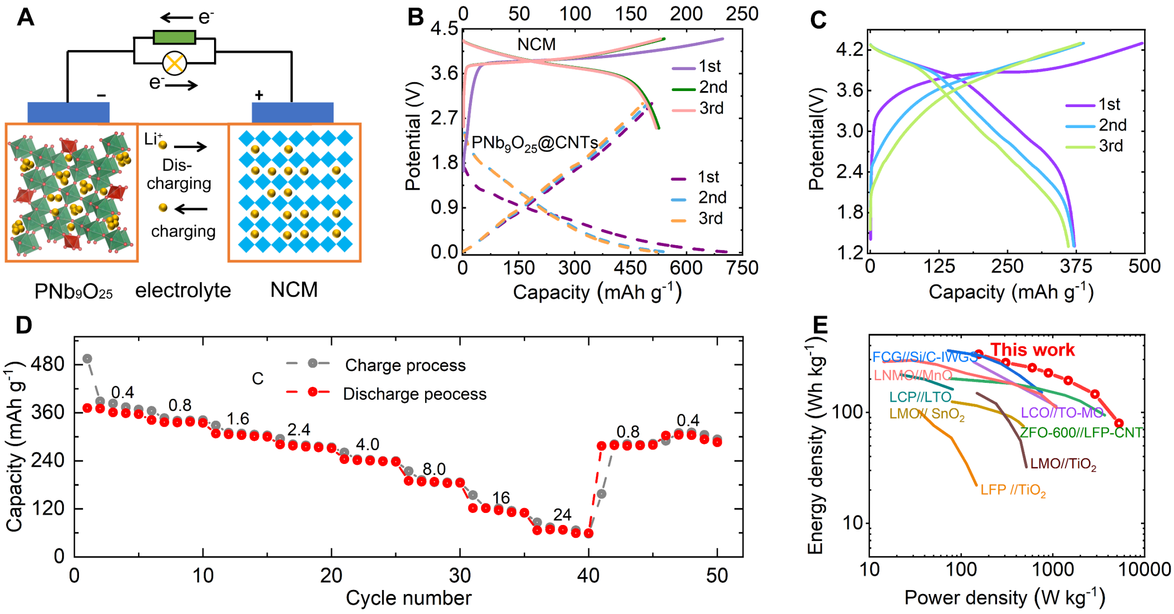

Fig. 6 | Full cell performance using the PNb_9O_{25} and NMC electrode. A. Illustration of full-cell construction. B, Representative charge-discharge voltage profiles of PNb_9O_{25}@CNTs and NCM at 0.05 A/g. C, Galvanostatic discharge and charge curves of PNb_9O_{25}@CNTs//NCM full cell at 0.4 C. D, Rate performance of PNb_9O_{25}@CNTs//NCM full cell based on anode mass. E, Ragone plot of the PNb_9O_{25}@CNTs//NCM full cell based on the total mass of the anode and cathode. The values reported for the other full batteries are added for comparison. (The energy density and power density of the literatures were also calculated based on the total mass of both cathode and anode materials)